Nanoscale

PAPER

View Article Online
View Journal | View Issue

Cite this: *Nanoscale*, 2023, **15**, 1739

Etching suppression as a means to Pt dendritic ultrathin nanosheets by seeded growth†

Deliang Yi,[a,b] Cécile Marcelot,[c] Idaline Romana,[b] Marine Tassé,[d] Pier-Francesco Fazzini,[a] Laurent Peres,[a] Nicolas Ratel-Ramond,[c] Philippe Decorse,[e] Bénédicte Warot-Fonrose,[c] Guillaume Viau,[a] Philippe Serp *[b] and Katerina Soulantica *[a]

Received 16th September 2022,
Accepted 6th December 2022

DOI: 10.1039/d2nr05105b

rsc.li/nanoscale

2D ultrathin metal nanostructures are emerging materials displaying distinct physical and chemical properties compared to their analogues of different dimensionalities. Nanosheets of fcc metals are intriguing, as their crystal structure does not favour a 2D configuration. Thanks to their increased surface-to-volume ratios and the optimal exposure of low-coordinated sites, 2D metal nanostructures can be advantageously exploited in catalysis. Synthesis approaches to ultrathin nanosheets of pure platinum are scarce compared to other noble metals and to Pt-based alloys. Here, we present the selective synthesis of Pt ultrathin nansosheets by a simple seeded-growth method. The most crucial point in our approach is the selective synthesis of Pt seeds comprising planar defects, a main driving force for the 2D growth of metals with fcc structure. Defect engineering is employed here, not in order to disintegrate, but for conserving the defect comprising seeds. This is achieved by *in situ* elimination of the principal etching agent, chloride, which is present in the $PtCl_2$ precursor. As a result of etching suppression, twinned nuclei, that are selectively formed during the early stage of nucleation, survive and grow to multipods comprising planar defects. Using the twinned multipods as seeds for the subsequent 2D overgrowth of Pt from Pt $(acac)_2$ yields ultrathin dendritic nanosheets, in which the planar defects are conserved. Using phenylacetylene hydrogenation as a model reaction of selective hydrogenation, we compared the performance of Pt nanosheets to that of a commercial Pt/C catalyst. The Pt nanosheets show better stability and much higher selectivity to styrene than the commercial Pt/C catalyst for comparable activity.

Introduction

The unique structural features of two dimensional (2D) ultrathin nanomaterials afford outstanding properties, exploitable in condensed matter physics, materials science, and chemistry. Excellent mechanic properties, optical transparency and the possibility to control the electronic properties by external stimuli are also characteristics of the 2D configuration. Finally, their high surface area makes them ideal candidates for many applications in which surface activity is crucial, such as catalysis and supercapacitors.[1] Among 2D nanomaterials, 2D ultrathin metal nanosheets (UMNS) have recently attracted the attention of the scientific community.[2–5] Compared to lamellar materials for which the adoption of a 2D configuration is favored, the 2D morphology in metals is rare and intriguing, as the non-directional metal bonds and the isotropic crystal structures, in which the majority of metals crystallize, do not favor the adoption of 2D shapes. The 2D morphology in metals is thermodynamically unfavorable due to its high surface energy. Despite their instability, free-standing monometallic,[6–8] as well as multi-metallic alloys and heterostructured UMNS,[8,9] have been synthesized by top-down and bottom-up strategies,[5] the latter constituting the most usually employed ones. The 2D morphology is achieved by employment of: (i) soft or hard templates to guide the 2D growth, (ii) shape directing capping agents that kinetically control the growth in 2D, and/or thermodynamically stabilize the extended exposed surfaces, (iii) 2D nanoparticles as seeds on the surface of which subsequent growth takes place with conservation of the 2D shape.[2–4,8]

[a]*Laboratoire de Physique et Chimie des Nano-Objets, UMR 5215 INSA, CNRS, UPS, Université de Toulouse, F-31077 Toulouse, France.*
E-mail: ksoulant@insa-toulouse.fr
[b]*LCC, CNRS-UPR 8241, ENSIACET, Université de Toulouse, 31030 Toulouse, France*
[c]*CEMES-CNRS, Université de Toulouse, CNRS, 29 rue Jeanne Marvig, 31055 Toulouse, France*
[d]*Laboratoire de Chimie de Coordination du CNRS, 205 route de Narbonne, F-31077 Toulouse, France*
[e]*ITODYS, UMR 7086, CNRS, Université de Paris, F-75013 Paris, France*

†Electronic supplementary information (ESI) available: Complementary TEM, HRTEM, EFTEM, AFM, catalytic results, XRD pattern, XPS deconvolution and associated tables. See DOI: https://doi.org/10.1039/d2nr05105b

Physical and chemical properties associated to the 2D ultrathin morphology,[2,7] which are not present in their 3D or 1D and 0D counterparts, make 2D-UMNS excellent candidates in the domains of sensing,[10] photothermal therapy,[11,12] and catalysis. While in the domain of electrocatalysis UMNS are being extensively studied,[9,11,13,14] their use in thermal heterogeneous catalysis is much less explored,[6,15–19] despite the fact that atom utilisation efficiency and improved mass activity of 2D-UMNS could be important advantages, particularly in the case of reactions catalyzed by noble metals for which cost-efficiency is mandatory.[4,20]

Defects, such as twin planes in fcc metals, can break the crystal structure symmetry, giving the possibility to expand the morphology repertoire beyond the isotropic shapes imposed by the fcc symmetry.[21,22] The origin of the 2D morphology in fcc metals (Ag, Au, Pd), is often associated to planar defects such as twin planes[23–26] appearing during nucleation or at later growth stages.[27] Grooves of plate-like seeds comprising {111} twin planes, constitute preferential sites for the addition of adatoms, thus leading to in-plane growth.[24,28,29] Planar defects giving rise to nanoprisms or nanoplates are thus considered as a major driving force for 2D growth. The internal structure of the seeds formed during nucleation is dictated both by thermodynamics and kinetics, and is determining for the morphology of the final nanocrystal.[21,30,31] However, small metal nanocrystals (≤5 nm) are subjected to structural fluctuations rendering the efficient control of the seed microstructure problematic. Consequently, controlling nanocrystal morphology through defect engineering is difficult, even if in some cases, manipulation of the precursor reduction kinetics allows seed structure control, through etching of the nuclei comprising defects.[30,32–35] It is well substantiated that twin boundaries are prone to etching, and oxidative etching is regularly employed in initial nucleation stages to control the shape of nanoparticles by selectively eliminating less stable, defect comprising nuclei, in syntheses that otherwise give rise to nanoparticles of mixed morphologies.[34,36] The opposite, that is, allowing the survival of only defect comprising nuclei is less common.[37,38] Defect engineering is not only a means to control nanocrystal morphology, but also their physical properties and chemical reactivity,[39–42] which is crucial for their implementation in catalysis. For example, it was recently shown, both theoretically and experimentally, that oxygen binds strongly to defect sites, and induces site-selective oxide formation in Ag and Pd nanocrystals containing planar defects.[43] Interestingly, the easier oxidation of defect-site atoms was also shown to play a critical role in the electrocatalytic oxidation of 5-hydroxylmethylfurfural by Ni-based multipods possessing branches of controllable thickness. In that case, an increase in the branch thickness led to an increase of the density of easily oxidizable defect sites, which in turn led to an improvement of the catalytic activity.[44]

Pt, one of the most widely used noble metals in catalysis, is a representative example for which the 2D configuration could be an efficient strategy toward improved catalytic performances and cost-efficiency, considering the high surface area and efficient utilization of metal active sites of the 2D nanostructures. Compared to other fcc metals such as Au, Ag and Pd, twinned Pt nanocrystals are less numerous.[45–48] This is likely due to the high twin boundary energies of Pt that does not favor twin nucleation.[34,49–51] The scarcity of Pt 2D nanocrystals comprising planar defects is even more striking. In fact, a small number of triangular Pt nanoplates with planar defects mixed with isotropic nanoparticles has been reported some years ago,[25] and more recently, twinned planar tripods have been formed as the major, albeit not the unique product, from H_2PtCl_6, poly(vinylpyrrolidone) (PVP) and KBr.[52] Interestingly the authors show that the controlled addition of HCl in their mixtures allows manipulation of the nanocrystal shapes, among which Pt platelets.

While several Pt-based UMNS have been synthesized by bottom-up methods,[13,53–55] pure Pt UMNS are rather scarce. Pt nanosheets have been obtained by intercalation and subsequent reduction by H_2 of $PtCl_4$ between graphite layers, which played the role of a hard template.[56] Very recently, a method employing silica-based hollow nanoreactors has also been employed in order to produce 2D Pt UMNS exposing {110} type facets, which have shown excellent performances in the hydrogen evolution reaction (HER).[57] Other bottom-up methods employ elaborated or home-made soft templates. For instance, lyotropic liquid crystals form 2D micelles, in which single-crystalline dendritic Pt UMNS have been synthesized at room temperature.[58–60] Recently, dendritic Pt UMNS of {110} type facets were prepared by using an amphiphilic surfactant, which acted as the structure directing agent.[61] Multilamellar liposomes have also been employed as templates for the interfacially directed formation of dendritic Pt-sheets,[62–64] and Pt-2D nanowheels have been prepared from bicelles.[65] In another work, it was proposed that the presence of a peptide and $AlCl_3$ induces the 2D assembly of isotropic nanocrystals to give polycrystalline Pt UMNS at room temperature.[66] In a different strategy, Liu *et al.* prepared Pt nanoplates exposing {111} facets by employing as a hard template Ag nanoplates comprising twin defects, which were used as seeds on which Pt was epitaxially grown. The Ag templates were subsequently etched away by HNO_3 from Ag@Pt core@shell nanoplates, leaving behind hollow Pt nanoplates.[67]

Here, we show that the selective synthesis of multipods comprising {111} planar defects from the reduction at room temperature of $PtCl_2$ by H_2 in the presence of octadecylamine (ODA) and sodium acetylacetonate (Na(acac)) is a key for the synthesis of Pt UMNS. We had previously shown that in the absence of Na(acac) the reaction yields single crystalline concave Pt nanocubes.[68] The presence of Na(acac) radically modifies the reaction outcome by enabling etching suppression *via* chloride elimination, and through this, the survival of twinned nuclei. These nuclei can thus grow to twinned multipods conserving their planar defects. The selective synthesis of twinned multipods and their use as seeds favors the formation of dentritic Pt UMNS by slow reduction of $Pt(acac)_2$ under H_2 in the presence of ODA, thanks to a preferential growth along the {111} twin planes of the seeds. This is the simplest

approach reported so far, since it does not demand specifically designed templates as it is the case for the pure Pt UMNS presented in previous works. It is also fundamentally different from the seeded growth methods that have been employed for the synthesis of M@Pt core@shell 2D-UMNS.[53,67,69] The dendritic UMNS thus obtained present {111} type basal planes, in contrast to the so far existing Pt nanosheets of similar morphology which present {110} type basal planes. Finally, as metal Pt UMNS are underexplored in selective hydrogenation reactions, we have tested them as catalysts in the selective hydrogenation of phenylacetylene (PhA) into styrene (ST). The selective hydrogenation of alkynes into alkenes is an important process from both the industrial and the academic points of view.[70] In industry, the removal of PhA, an impurity in ST, by selective hydrogenation, is crucial, because PhA poisons and deactivates polymerization catalysts in polystyrene production plants. The advantage of this process is that the undesired alkyne is directly converted into the target alkene.[71] Achieving high selectivity to the targeted alkene at high alkyne conversions without over-hydrogenation is a key step in the polymer and fine chemical industries.[70,71] For this reaction, the catalytic performances of the transition metal strongly depend on its electronic structure, and unpromoted Pt catalysts are not selective because they bind strongly, both C≡C and C=C,[72] provoking overhydrogenation of alkynes to alkanes.[70]

Experimental

In order to exclude the influence of oxygen and of ambient humidity, the syntheses of the seeds were performed under inert conditions, using vacuum-line and glove-box techniques. Toluene (99%) was purified by a solvent purifier (Innovative Technology Purification System), degassed by Ar bubbling, and then kept in the glovebox. Thus, the presence of moisture and air was strictly excluded from the system during the seed synthesis. Seed purification was performed under ambient conditions. The platinum chloride ($PtCl_2$, 98%) was purchased from Alfa Aesar. $PtCl_2$ only from freshly opened containers should be used, as formation of Pt nanoparticles has been detected in $PtCl_2$ vials opened for a long time. Platinum acetylacetonate ($Pt(acac)_2$, 98%) was purchased from Strem, sodium acetylacetonate (Na(acac), 95%) from Alfa Aesar, octadecylamine (97%) from Sigma Aldrich, and a commercial Pt/C catalyst was purchased from Aldrich (206931-10G), 5 wt% loading, activated carbon support.

Synthesis of Pt seeds

For a typical synthesis of Pt seeds in a glove box, 16 mg (0.06 mmol) of $PtCl_2$ (98%), 60 mg (0.5 mmol) of Na(acac) (sodium 2,4-pentanedionate hydrate), 400 mg ODA (octadecylamine, 1.5 mmol) and 7 mL of toluene were mixed in a Fischer–Porter bottle. The bottle was closed, removed from the glove box and sonicated for 10 min, giving rise to a yellow-brown turbid suspension. The Ar was evacuated and the Fischer–Porter bottle was charged with H_2 (3 bar) under stirring. The mixture was let to react for 24 hours under stirring (400 rpm) in a double-wall support, thermostated at 20 °C. After the end of the reaction, the Fischer–Porter reactor was evacuated and the suspension was centrifuged at 10 000 rpm for 10 min and the supernatant was removed. The product was washed twice with 20 mL ethanol (96%) and three times with 20 mL toluene. After each solvent addition, the mixture was sonicated for 10 min. The final product was dispersed in 10 mL toluene giving rise to a suspension of 1 mg mL^{-1} (Pt = 34.1 wt% as determined by TGA analysis of a 10 mg dried sample). After sonication of this dispersion for 10 min, aliquots were used as seeds for the subsequent growth of Pt UMNS.

Synthesis of Pt nanosheets

For a typical synthesis of Pt UMNS in a glove box, in a Fischer–Porter bottle, $Pt(acac)_2$ (24 mg, 0.06 mmol), and octadecylamine (400 mg, 1.5 mmol) were introduced in toluene (5.8 mL), giving rise to a bright yellow solution. A Pt seed aliquot (1.2 mL, 1 mg mL^{-1}, 2.1×10^{-3} mmol of Pt) was added to the mixture, which was then sonicated for 10 minutes. The Fischer–Porter bottle was evacuated and then charged with 3 bars H_2 under stirring. After 7 minutes, the reactor was closed and the mixture was let to react for 4 days under stirring (400 rpm) in a double-wall support, thermostated at 20 °C. Once the reaction completed, the Fischer–Porter bottle was evacuated and the mixture was centrifuged for 10 minutes at 10 000 rpm. The supernatant was removed, and 20 mL toluene were added, followed by centrifugation for 10 minutes at 10 000 rpm. This step was repeated once. Then, 20 mL of toluene were added and the mixture was sonicated for 10 min, and the supernatant was removed after letting the mixture to decant. This process was repeated for 3 times. This last step allowed discarding the few small nanocubes that are produced as a byproduct. The precipitate was washed 1 time with pentane and vacuum dried and stored under ambient conditions. The Pt content was analyzed by ICP to be 81.2 wt%.

Characterization

Conventional transmission electron microscopy (TEM) characterizations were performed on a JEOL JEM 1011 CX-T electron microscope operating at 100 kV with a point resolution of 4.5 Å. The particle size and morphology were evaluated through TEM by measurement of at least 200 objects. High-resolution transmission electron microscopy (HRTEM) and energy-filtered transmission electron microscopy (EFTEM) were performed on a Cs corrected Hitachi HF3300 microscope (I2TEM) operated at 300 kV with a Gatan imaging filter, and on a JEOL cold FEG ARM microscope operated at 200 kV.

Atomic force microscopy (AFM) was performed on a SmartsSPM-1000, AIST-NT microscope, which was used to explore the surface morphology of the samples. Topography was measured in tapping mode with a silicon tip of 15 μm length and 8 nm radius of curvature. AFM topography images of the objects are obtained by a dispersion of UMNS in a mixture of toluene/pentane and deposited on glass substrates.

The objects thickness were estimated by measuring their profile with the help of Gwyddion software. The measurements were taken at different locations on the surface, and the scan areas were between 10 and 0.5 μm.

ICP analyses were performed by Kolbe. TGA analyses were performed on a METTLER ATG-DSC3+ instrument.

X-Ray diffraction experiments have been performed on a Malvern Panalytical Empyrean diffractometer, equipped with a Co anticathode X-ray source, a Bragg–Brentano HD mirror, and a PIXCel1D detector. The sample consists in a powder drop-casted on a zero-background Si support. Data have been acquired between 2θ values of 40° and 110° with an angular step of 0.02° and 1 s exposure per step in continuous mode.

X-ray photoelectron spectroscopy (XPS) spectra were recorded from samples prepared by depositing on a Si wafer a few drops of the suspended solids followed by solvent evaporation. The spectra were recorded using a K-alpha plus system (Thermo Fisher Scientific, East-Grinstead, UK) fitted with a micro-focused and monochromatic Al Kα X-ray source (1486.6 eV, spot size of 400 μm). The spectrometer pass energy was set to 150 and 40 eV for the survey and the narrow high-resolution regions, respectively.

Catalytic tests

For the catalytic tests, exactly weighted amounts of dried Pt UMNS were dispersed in 10 mL of solvent to prepare a mother suspension from which aliquots of exactly measured volumes are used in each catalytic run. The metal content of the weighted samples was known from ICP analysis of the dried UMNS. The catalytic reactions were performed in a high-pressure stainless steel autoclave connected to a gas ballast and working at constant pressure. After introduction of the reactants, the autoclave was sealed up and purged with H_2 3 times. The hydrogenation experiments were carried out at a stirring rate of 1200 rpm under 5 bar H_2 at 25 °C.

In a typical experiment, Pt UMNS (0.62 mg, Pt = 81.2 wt%), 410 mg of phenylacetylene, 70 mg decane as internal standard and 20 mL of THF were added in the autoclave. The mixture was sonicated for 10 min. The autoclave was closed and purged with 3 bar H_2 3 times, and finally filled with 5 bar H_2. The temperature was controlled at 25 °C, and the stirring speed was kept at 1200 rpm. Samples were removed from the autoclave at regular intervals and were analyzed on a PerkinElmer (Clarus 580) gas chromatograph equipped with an Elite-5MS capillary column (30 m × 0.32 × 0.25 μm) and with a flame ionization detector. The same procedure was applied for the tests with 10 mg of the commercial 5 wt% Pt/C catalyst.

The conversion and the selectivity were calculated from the following equations:

$$\mathrm{Conv}\% = (n_{\mathrm{initial}} - n_{\mathrm{final}})/n_{\mathrm{initial}} \times 100\%,$$

$$S_x\% = n_x/n_{\mathrm{product}} \times 100\%,$$

where, n_{initial}: mol of phenylacetylene introduced; n_{final}: mol of phenylacetylene remaining; n_x: mol of product x; n_{product}: total amount of products (mol).

The activity was calculated from the following relationship:

$$\mathrm{Activity} = \mathrm{mol}_{\mathrm{PhA}}\ \mathrm{mol}_{\mathrm{metal}}{}^{-1}\ \mathrm{h}^{-1}$$

where, $\mathrm{mol}_{\mathrm{PhA}}$: mol of phenylacetylene converted; $\mathrm{mol}_{\mathrm{metal}}$: mol of total Pt amount.

Results and discussion

Synthesis and characterization

In a previous work,[68] we showed that the reduction of $PtCl_2$ under H_2 at 20 °C in the presence of octadecylamine (ODA) results in the slow formation of single crystalline concave Pt nanocubes exposing {110} type facets, which grow from cubic seeds through deposition of Pt adatoms on the nanocube corners and their subsequent diffusion along the nanocube edges (Fig. S1†). The simple replacement of $PtCl_2$ by $Pt(acac)_2$ (acac = acetylacetonate) leeds to the slow formation of nano-objects of mixed morphology, among which, few dendritic 2D nanostructures (Fig. 1). High resolution transmission electron microscopy (HRTEM) observation of the multibranched nano-objects shows that they correspond to fcc Pt nanosheets generally observed along a [111] zone axis. In this orientation, fast Fourier transform (FFT) of a large area shows a small angular enlargement of the {220} reflection spots, due to a slight misalignment of the crystallographic orientation between different sections of the nanosheet, as confirmed by the FFT of small areas on different pods (Fig. 1c and d). The FFT also reveal the presence of 1/3 {422} reflexions, which are forbidden in a perfect fcc crystal, and are characteristic of the presence of at least one twin plane running parallel to {111} faces of platelet-shaped nano-objects.[46,73] Therefore, under conditions in which $PtCl_2$ forms single crystals exclusively,[68] $Pt(acac)_2$ induces the formation of nanostructures dominated by twin defects.

The striking difference between the results obtained with the two precursors, incited us to examine the influence of acac in the formation of twinned nanostructures by using $PtCl_2$ as a precursor, but in the presence of sodium acetylacetonate (Na(acac)) as a source of acetylacetonate. The reaction under H_2 of $PtCl_2$, ODA and Na(acac) ($PtCl_2$/Na(acac)/ODA = 1/8/25) at 20 °C gives rise to dendritic Pt multipods after 24 hours of reaction (Fig. 2a and b). HRTEM observations confirmed the expected fcc crystal structure of Pt. Interestingly, whenever the branch orientation with respect to the beam direction was favorable, a single {111} twin plane was evidenced (Fig. 2c). Branches oriented along the [111] zone axis were also frequently observed (Fig. 2d). These observations point toward the formation of dentrites composed of thin branches comprising {111} twin planes.

The time dependent morphological evolution of these multipods shows the initial formation of nanostructures presenting one, two or three wormlike branches of about 10 nm length, 1.5–2.0 nm diameter, terminating to enlarged tips

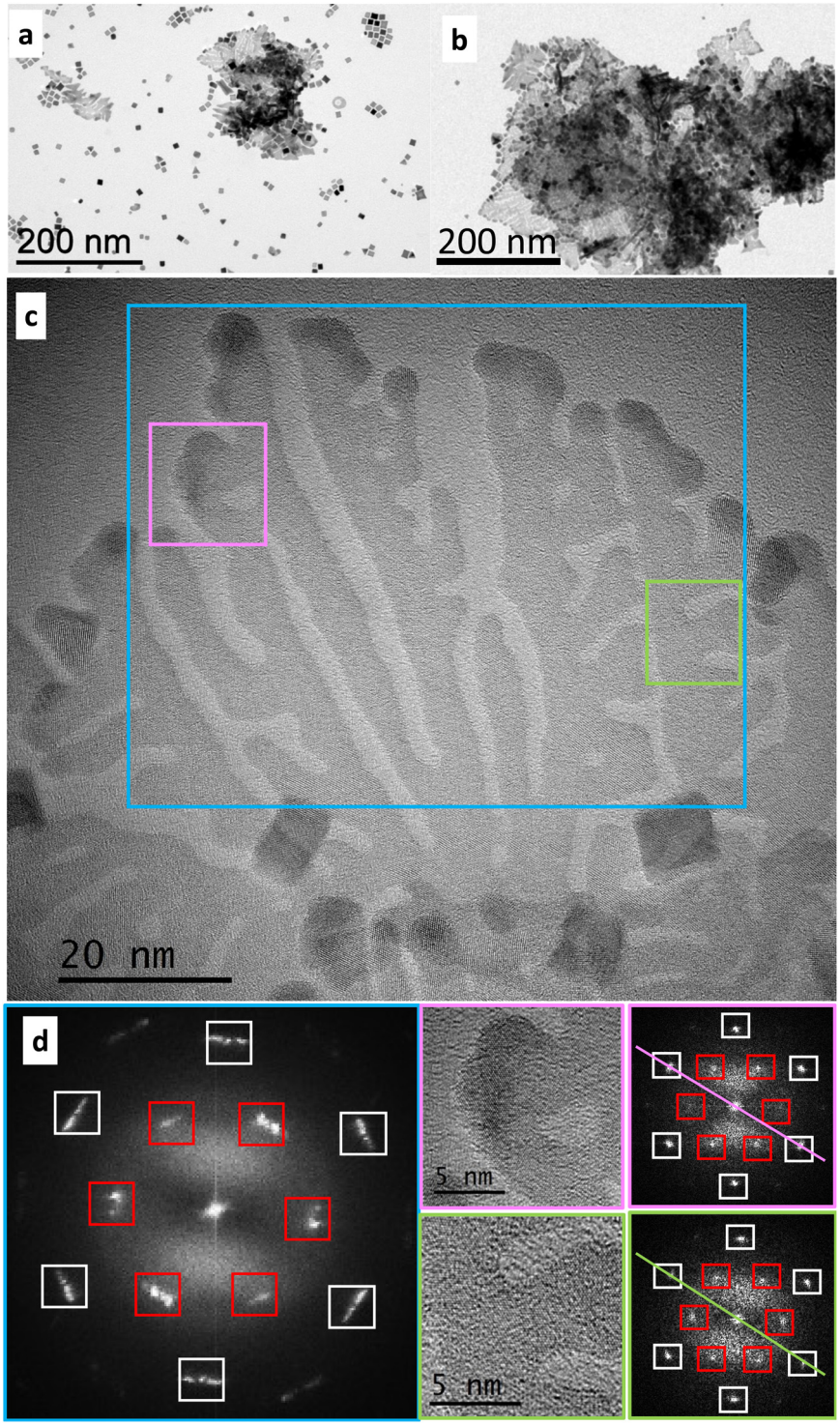

Fig. 1 Nanostructures obtained by reduction by H_2 (3 bar) of $Pt(acac)_2$ in the presence of ODA at 20 °C. (a) 4 days reaction. (b) 7 days reaction. (c) HRTEM image of a Pt UMNS obtained after 7 days reaction, and (d) FFT of the areas marked by the frames with corresponding colours in c. The lines joining antidiametric {220} reflection spots in the selected small areas illustrate a small misalignment between the areas, which is responsible for the angular enlargement observed in the FFT of the area framed in cyan. The spots due to the {220} reflections are in white frames and the ones due to the 1/3 {422} forbidden reflexions are in red frames. Zone axis: [111].

(Fig. S2a–c†). Judging from their increased contrast, the tips seem to be thicker. Letting the reaction proceed for several days (Fig. S3†), induces aggregation, which makes subsequent dispersion of the seeds difficult. After 24 hours, these nanostructures evolve into dendritic nano-objects, most likely through multiple branching events. The predominance of

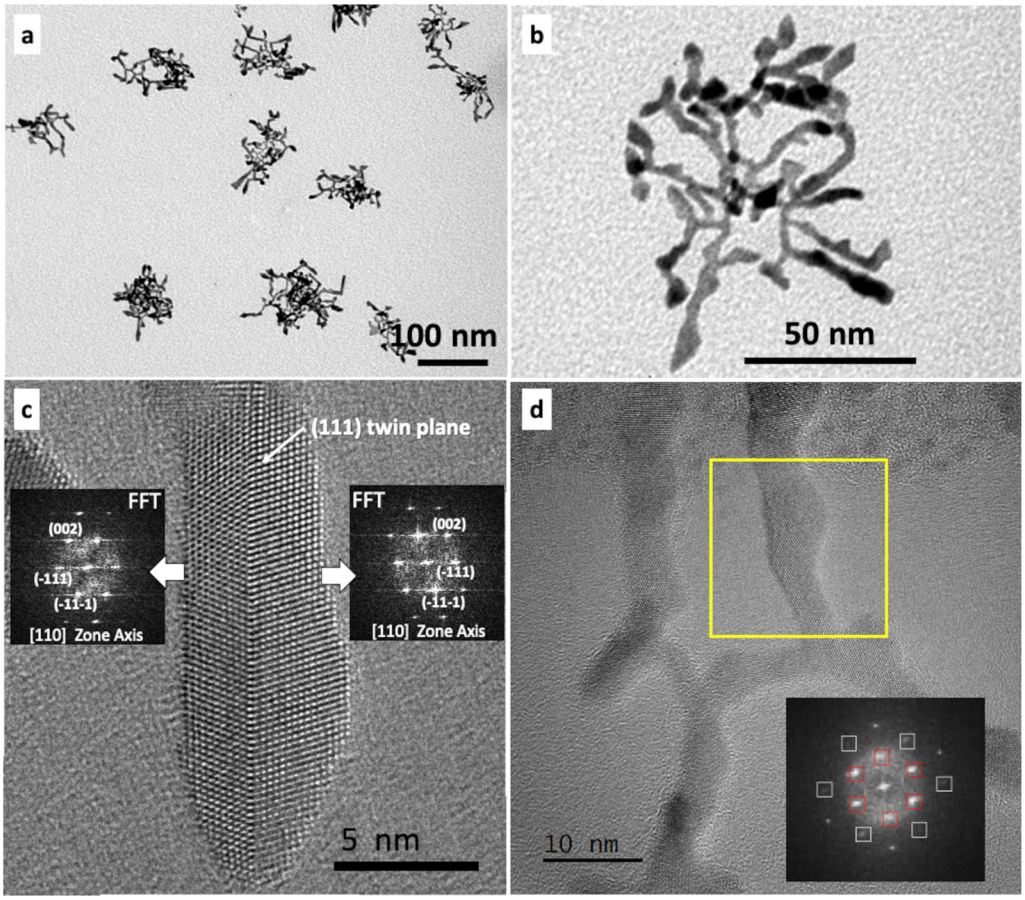

Fig. 2 Electron microscopy of multipods resulting after 24 h reduction by H_2 (3 bar) of $PtCl_2$ at 20 °C, in the presence of ODA and Na(acac). (a) General view. (b) An isolated nano-object at higher magnification. (c) HRTEM micrograph of a branch (edge-on view) in which the twin plane is indicated by the white arrow. Zone axis: [110]. The {002} and {111} reticular distances of 1.95 Å and 2.26 Å, respectively, were measured from the FFT and correspond to the bulk distances (JCPDS Pt file 00-004-0802); (d) HRTEM micrograph of a Pt multipod oriented along the [111] zone axis. In the inset, the corresponding FFT of the area marked in the HRTEM image by the yellow frame. In the FFT the spots due to the {220} reflections are in white frames and the spots of the 1/3 {422} forbidden reflexions are in red frames.

three-branched specimens at early reaction times (Fig. S2†) suggests that three-fold symmetry twinned seeds grow by addition of Pt along the {111} twin planes, either on one, two or three of their tips. Outgrown branches are then subjected to additional branching events to give the final multipods, with planar defect conservation. HRTEM analysis of an appropriately oriented nano-object obtained after 8 hours of reaction shows the presence of a twin plane (Fig. S4†).

Since in the absence of seeds, the reduction of $Pt(acac)_2$ by H_2 in the presence of ODA forms only few UMNS as a minor morphology in a mixture of cuboidal nano-objects (nanocubes and concave nanocubes) (Fig. 1), we expected that, adding the multipods as seeds already including twin defects in the reaction medium, would enhance the shape selectivity to Pt UMNS. Combined to the mild reaction conditions employed in order to limit new nucleation events, the presence of these seeds should favor the growth by heterogeneous nucleation, which could proceed with retention of the planar defects of the seeds. Indeed, the introduction of the multipod seeds in a growth solution containing $Pt(acac)_2$ and ODA gives rise to dendritic Pt UMNS after 4 days reaction under H_2 at 20 °C (Fig. 3a–c). The majority of the UMNS have diameters that extend over 100–500 nm and speciments of either triangular or round contours are formed at the same time (Fig. S5†). Most of the times, several UMNS form layers of overlapping individual sheets and folded UMNS are often observed.

X-Ray diffraction of the isolated powder showed that the particles crystallize with the fcc structure (Fig. S6†), and HRTEM observations showed that the Pt UMNS are generally observed along a [111] zone axis (Fig. 3d and e). Fig. 3e shows the FFT recorded from the large area of the UMNS shown in Fig. 3d. This pattern, displaying distinct spots, corresponds to a single crystalline configuration and not to a polycrystalline nano-object, even if it involves several branches of the particle. This proves a very good coherence of the crystalline orientation from one branch to another with only a slight misorientation in the plane perpendicular to the zone axis. This is indicated by the small angular enlargement of the spots, as in the case of the scarce nanosheets formed in the absence of preformed sheets by $Pt(acac)_2$ and ODA (Fig. 1c and d). Additionally, the

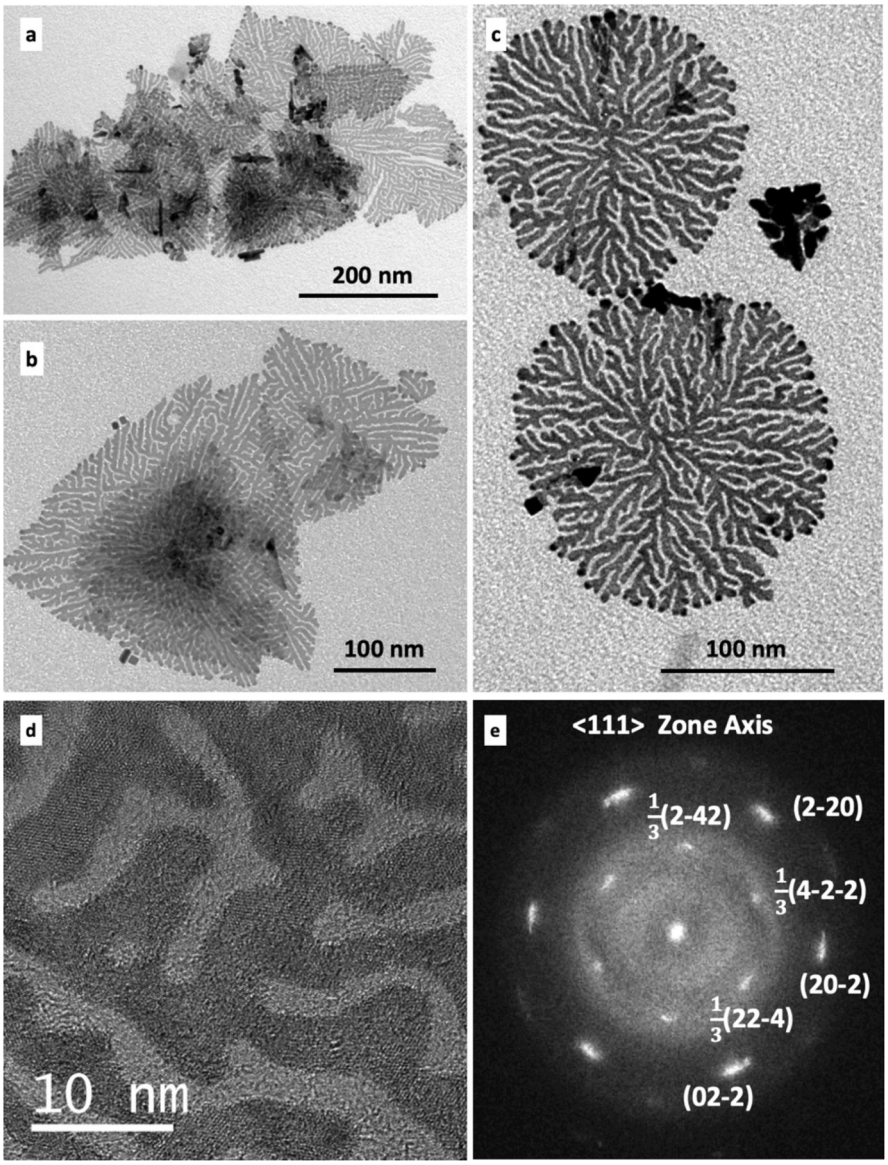

Fig. 3 Dendritic Pt UMNS produced after 4 days reaction. (a) Lower magnification image: the UMNS overlap, and folded UMNS appear as higher contrast areas. (b) Image of triangularly shaped overlapping nanosheets. (c) Round contour Pt UMNS. (d) HRTEM of a UMNS. (e) The corresponding FTT indicating the spots due to the {220} reflections and the spots of the 1/3 {422} forbidden reflexions.

FFT displays six 1/3 {422} forbidden reflexions, indicating the presence of {111} type twin planes running parallel to the basal UMNS planes (Fig. 3e).

TEM observation of samples obtained after stopping the reaction at various time intervals demonstrates that the dentrites gradually evolve toward UMNS (Fig. S7†). As the UMNS grow from the center toward the periphery, multiple branching events in the growing plane fill the 2D space between the branches, which however do not fuse together, thus forming channels. After 4 days, the UMNS are fully grown and extending the reaction time to 7 days seems to slightly thicken the extremities of the branches. Evaluation of the relative thickness by energy filtered transmission electron microscopy (EFTEM) indicates that it is about 1 nm, that is, about 4–5 Pt layers thick (Fig. S8a and b†). Atomic force microscopy (AFM) measurements on whole nanosheets corroborate the EFTEM result (Fig. S8c†).

XPS analyses (Fig. 4), relevant both for rationalizing the formation of the nanostructures and the catalysis results,[74] have been performed to obtain information on the surface chemistry of the multipod seeds and Pt UMNS. The Pt UMNS present a broad N 1s peak (Fig. 4a) that can be resolved into three components (deconvolution in Fig. S9a and fitting results in Table S1†). The major N 1s signal at 401.2 eV corresponds to an ammonium moiety ($-NH_3^+$, 401.3–401.7 eV).[75,76] The peak at 399.6 eV corresponds well to what might be expected for a nitrogen atom donating electron density to the Pt surface *via* its lone pair (399.5–399.6 eV),[77,78] but could also

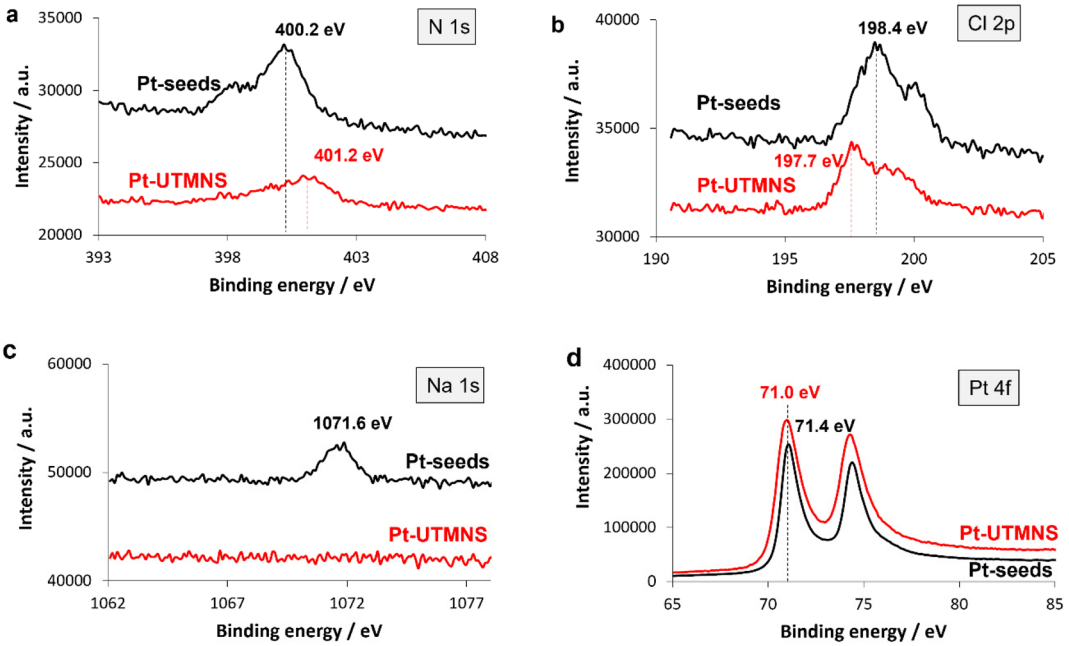

Fig. 4 High resolution XPS spectra of Pt UMNS and Pt seeds. (a) XPS spectra in the N 1s region. (b) XPS spectra in the Cl 2p region. (c) XPS spectra in the Na 1s region and (d) XPS spectra in the Pt 4f region.

correspond to free ODA (399.2–399.4 eV),[76] which points toward a moderate charge transfer from the ligand to the metal. The peak at 398.0 eV could correspond to an imine,[77] formed by the condensation between the ODA and acac.[79] The N 1s spectrum of the Pt seeds is shown on Fig. 4a (deconvolutions in Fig. S10a and fitting results listed in Table S1†). The major species is located at 400.2 eV (coordinated amine), a minor peak at 398.2 eV corresponds to electron rich N species, and the absence of any contribution at 401.2 eV suggests that the nitrogen species are not protonated on the Pt seeds.

Despite the fact that the Pt UNMS growth solution was composed only of [Pt(acac)$_2$] and ODA, Cl was detected by XPS (Fig. 4b). The only explanation for the presence of Cl on the Pt UNMS is its presence on the multipod seeds, which are prepared from the $PtCl_2$ precursor. Indeed, the XPS analysis of the Pt seeds shows the presence of Cl (Fig. 4b). The Cl 2p spectrum of the Pt UMNS) was deconvoluted by fitting two spin orbit split peaks ($2p_{1/2}$ and $2p_{3/2}$) for each of the different chemical states of chlorine (deconvolution in Fig. S9b and fitting results in Table S2†). The major peak (83 at%), appears at a $2p_{3/2}$ binding energy (BE) of 197.7 eV, indicating the presence of ionic chloride species, which could be present both as a counter ion of the ammonium (BE = 196.6 eV)[80] and coordinated on the Pt surface (BE at 198.2–198.6 eV).[81] The second peak with a $2p_{3/2}$ BE at 200 eV (17 at%) indicates the presence of more covalent chlorine species. Since Cl species on Pt (metal or oxide) have been reported at BE as high as 199.2–200 eV,[82–85] we have attributed this peak to Cl adsorbed on PtO, which has been formed by exposure of the sample to air. The Cl 2p spectrum of the Pt seeds (Fig. 4b) shows the presence of a single ionic chloride contribution with $2p_{3/2}$ BE peak at 198.4 eV (deconvolutions are shown in Fig. S10b and fitting results listed in Table S2†), consistent with the presence of a single bonding environment for the Cl atoms.[82,86] Since no ammonium was detected for the Pt seeds, we can exclude any contribution from ammonium chloride. NaCl (BE at 198.7 eV) should contribute to this peak, since Na (BE at 1071.6 eV) was detected in the case of the Pt seeds (Fig. 4c). It is also possible that Cl associated to Pt contributes to this peak (BE at 198.3–198.5 eV for 1–3 nm Pt nanoparticles).[81]

The C 1s spectrum of the UMNS is shown on Fig. S11a and b (fitting results listed in Table S3†). The more intense peak (C_A) at 284.8 eV is related to aliphatic sp^3 C (C–C/C–H from amine or acac). The second peak (C_B) at 286.2 eV can be attributed to contributions of C–O, C–N and C=N species (from acac,[87,88] amine,[89,90] and imine).[91] Finally, the peak at 288 eV (C_C) is attributed to the C=O group from acac.[87] The C 1s spectrum of the Pt seeds is shown on Fig. S11c and d (fitting results listed in Table S3†). As for the UMNS aliphatic sp^3 carbon (C_A) is present. The main difference arises from a shift of the C_B and C_C peaks from 286.2 to 286.4 eV (C_B) and from 288.0 to 288.5 eV (C_C). For the C_B peak, this shift can be attributed to different contributions of the three C–O, C–N and C=N species, whereas for the C_C peak it could be related to a different environment of the acetylacetonate ion. The BE of the carbonyl group of the acac ligand coordinated on Pt has been measured at 288.5 eV,[88] which corresponds well to what we found for the seeds. The lower BE measured for the UMNS could be related to the presence of the acac as anion of the ammonium salt, which is not present on Pt seeds.

The Pt 4f spectrum of the UMNS is shown on Fig. 4d (see Fig. S9c for deconvolution and Table S4† for fitting results).

The peaks at 70.9 eV (61 at%), 71.9 (28 at%), and 73.4 eV (11 at%) correspond to the Pt $4f_{7/2}$ peaks of Pt^0, $Pt^{\delta+}$ (Pt–Cl species or Pt-acac),[78,82] and Pt^{2+} (PtO) respectively.[92] The Pt 4f spectrum of the Pt seeds (deconvolution are shown in Fig. S10c and fitting results listed in Table S4†) is similar to the one of the UMNS (Fig. 4d), pointing to a similar electronic effect of the surrounding ligands in both samples. We noticed only the absence of surface oxidation due to prolonged air exposure for the Pt seeds (no PtO peak at 73.4 eV).

From these XPS analyses, some important information is obtained: first, Cl ions coming from the Pt seeds are present on the UMNS. Second, octadecylamonium ions are absent from the seeds but present on the UMNS. Third, Na is absent from the UMNS but present on the seeds, which points toward NaCl being present on the seeds as an impurity. Fourth, it is clear that, even at room temperature, side reactions between the acac and the amine can take place as it has already been reported for nanoparticle syntheses employing metal acetylacetonates with primary amines.[79] Even if the reaction conditions were not the same as in the present work, several organic products have been detected in the case of reactions of oleylamine with $Pt(acac)_2$,[93] or $Ni(acac)_2$.[79] Schiff condensation of NH_2 and C═O was also reported during the grafting of various $M(acac)_2$ precursors on amine functionalized silica.[94] Finally, a moderate charge transfer from the amine to the metal has been evidenced.

Mechanistic considerations

The information obtained from our data allows an insight into the processes taking place during the two steps leading to the UMNS: (i) the formation of the twinned multipods, and (ii) the growth of UMNS using the multipods as seeds. As we have seen, employing the twinned multipods as seeds is crucial for greatly improving the shape selectivity to UMNS. Therefore, the synthesis of the dendritic twinned seeds merits further attention, as it is a key for increasing the UMNS shape yield in the second step.

In order to better rationalize our results, it is important to identify the essential conditions that allow planar defects to dominate in the multipod seeds. The origin of the striking difference between the nano-objects formed in the presence of Na(acac) (twinned multipods) and the ones in it absence (single crystalline concave nanocubes)[68] from the reduction of $PtCl_2$ by H_2 in the presence of ODA is the base for determining the most important driving force for the selective formation of twinned multipods, which are crucial for the development of the UMNS.

Due to the very limited solubility of $PtCl_2$ and Na(acac) in toluene, in a first step, $PtCl_2$ should slowly provide soluble Pt species through Cl-bridge splitting by ODA. We presume that $PtCl_2(ODA)_2$ is the most probable initially formed Pt species. Complexes involving acac and mixed ODA-acac compounds can be formed,[95] however the poor solubility of Na(acac) most likely prevents acac coordination, at least at the beginning of the reaction. Reduction of the soluble intermediate(s) by H_2, necessarily involves elimination of the chloride, as HCl, and it is well substantiated in the literature that HCl can dissolve nuclei incorporating defects.[22,34,35,96] This is in fact what happens in the case of the reaction between $PtCl_2$ and HDA where only single crystalline concave cubes are produced: chloride-induced etching disintegrates metastable twinned nuclei, and allows formation of more stable single crystalline ones that evolve to concave nanocubes (Fig. S1†).[68] However, when Na(acac) is present, the released HCl is efficiently put out of circulation through formation of insoluble NaCl, which is corroborated by the XPS analysis of the multipods, and acacH. Efficient scavenging of the Cl ions switches off the possibility of etching, and allows the survival of the twinned nuclei and their growth beyond a critical size, because the reaction pathway that ripens twinned nuclei to single crystals is blocked. Twinned nuclei subsequently grow to multipods, which conserve the twin defects.

While switching etching off explains the persistence of twinned nuclei that then grow to multipods, it cannot explain the complete absence of single crystalline specimen in the reaction product. The birth of defects during nanocrystal nucleation is poorly understood and mixtures of different nuclei can coexist in the early nucleation stage.[97–99] However, our results suggest that nuclei with planar defects is the exclusive product during the early nucleation stage. If this hypothesis is correct, then oxidative etching should be the unique pathway to more stable shapes, such as cuboctahedrons, which then evolve to cuboids. Thus, increasing the temperature should not affect the reaction outcome.[31,34] In order to verify this, we performed at 100 °C the standard reaction that gives rise to multibranched twinned seeds at 20 °C. As shown in Fig. S12,† small multipods resembling to the wormlike seeds obtained at early reaction times at 20 °C are the only products of the reaction. Therefore, provided that etching is the main mechanism by which evolution of the nuclei takes place during the nucleation step, *in situ* suppression of the etching process offers also the opportunity to obtain information on the internal structure of the initially formed metastable nuclei.

The presence of Na(acac) in excess with respect to $PtCl_2$ is necessary for the twinned multipods to be selectively formed. Control experiments performed in the presence of different $PtCl_2$/Na(acac) ratios are shown in Fig. S13a–c.† Reducing the Na(acac)/$PtCl_2$ ratio increases the number of nano-objects with cuboidal symmetry at the expense of dendritic nano-objects, and when a stoichiometric ratio ($PtCl_2$/Na(acac) = 2) is employed (Fig. S13c†), very few multipods are formed. These results point towards a competition between Na(acac) and ODA for chloride. ODA, which is in large excess in solution, could form $ODAH^+Cl^-$, which is acidic enough to etch away twinned nuclei produced during the early nucleation stages.[100] We assume that, in the absence of a high excess of Na(acac), the Cl ions of $ODAH^+Cl^-$ have the possibility to etch away twinned nuclei giving the opportunity to the system to attain the thermodynamically favored shapes, before elimination from the solution of the Cl^- as NaCl is completed.

Considering the second step of the reaction, that is, the UMNS formation in the presence of twinned seeds, it is worth

considering first what is happening with $Pt(acac)_2$ and ODA in the absence of seeds (Fig. 1). Interestingly, the formation of a mixture of cubes and scarce UMNS indicates that under these conditions, twinned nuclei are indeed formed, but only few overpass the critical size after which they cannot be completely dissolved. This indicates that etching is operating in this case also, however it is less efficient than the one induced by Cl. When only $Pt(acac)_2$ and ODA are used, the only possible etchant is the acac ions that may be present as the anion of octadecylammonium.[101] Thus, while a few twinned nuclei survive to grow to UMNS, the majority of them does not attain the critical size. Even if it is mild, the etching induced by $acac^-$ allows the energy barrier to the stable nuclei to be overpassed with time, yielding cuboidal crystals as the major product. Indeed, the fact that the UMNS produced from the seeded growth with multipods seem to have more homogeneous thickness and they are thinner than the tips of the seeds from which they grow (Fig. 1c), is in agreement with a mild etching process by acac ions.

Scheme 1 summarizes the proposed nucleation pathways, and the different types of seeds favored in each case. When only $PtCl_2$ and ODA are present (Scheme 1a), the Cl ions liberated remain in the reaction medium and etch away the kinetically favored twinned nuclei as soon as they appear. As the reaction proceeds, the thermodynamically favored defect-free nuclei, represented here as cubes, are formed, and after subsequent growth, they evolve to concave cubes as described by Peres *et al.*[68] Addition of Na(acac) in sufficient amounts in the reaction medium (Scheme 1b) traps the Cl ions as NaCl. Due to the insolubility of NaCl, there is no possibility of etching. Only the kinetic product (twinned nuclei) survives and evolves to the twinned multipods. Scheme 1c illustrates the situation where only $Pt(acac)_2$ and ODA are used. In this case, only acac ions of mild etching ability are present. A competition between the kinetic and the thermodynamic product is possible. Only few twinned nuclei have the possibility to attain the critical size beyond which complete dissolution is not possible anymore, and grow to UMNS. The majority of the seeds is transformed to the most stable product that after growth are present as nanoparticles of cubic symmetry.

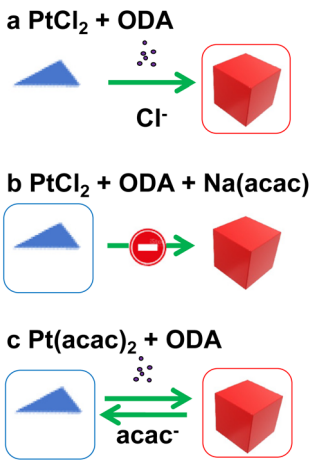

Scheme 1 Qualitative representation of the nucleation pathways for each case discussed. The framed nano-objects correspond to the structures that survive after the nucleation step. Twinned seeds are represented as blue triangles and defect-free seeds as red cubes. (a) $PtCl_2$ in the presence of ODA. The Cl ions liberated remain in the reaction medium and etch away the kinetically favored twinned nuclei. (b) $PtCl_2$ in the presence of ODA and Na(acac). Na(acac) eliminates the Cl ions as insoluble NaCl. Etching suppression allows survival of the kinetically favored twinned nuclei, which evolve to twinned multipods. (c) $Pt(acac)_2$ in the presence of ODA. Only acac ions of mild etching ability are present. A competition between the kinetic and the thermodynamic product is possible.

The last nucleation pathway ($Pt(acac)_2$/ODA) is important for understanding the seeded growth of UMNS by introduction of seeds in the system. Here also, some cubes are still produced due to the mild etching process by the acac ions and probably due to the presence of chloride residues on the seeds and as $ODAH^+Cl^-$, as indicated by the XPS of the UMNS. However, when the reaction is performed at low temperature, heterogeneous nucleation on the seeds is favored, etching is limited and the kinetic product (UMNS) is favored. The importance of employing very mild temperature in this second step is reflected in the dramatic modification of the resulting nanoobjects morphology upon slightly increasing the temperature. Indeed, 16 h reaction at 40 °C results in the formation of a high number of thermodynamically more stable nanocrystals of diverse shapes (Fig. S14a†). On the other hand, reducing the temperature to 10 °C, does not allow the reaction to proceed at an appreciable rate (Fig. S14b†).

We have evidenced the determining role of the chloride on the first step of the reaction, that is the seed growth. However, Cl, acac and ODA and their derivatives are also present on the surface of the seeds and the UMNS formed from these seeds. The multiple roles that halides may play have been the subject of several studies.[96,102–104] Apart from controlling the reduction kinetics, the ligands, as well as their reaction products detected by XPS, may also play important roles in the stabilization of the exposed facets. For instance, the length of the amine affects the shape of both the seeds and the UMNS (Fig. S15†), with the shorter ligands not being well adapted to produce UMNS. We speculate that long chain amines can be organized parallel to each other on the surface of the UMNS, thus avoiding extensive etching of the UMNS by acac.

To summarize, we have shown that: (i) Cl^- is detrimental to the survival of the twinned nuclei, which are formed as the exclusive product in the early nucleation step from $PtCl_2$ and ODA, (ii) the elimination of Cl^- as insoluble NaCl is the key for the selective formation of twinned seeds. (iii) Etching suppression allows an insight to the internal structure of the early nucleation products, (iv) $acac^-$ as a mild etching agent is responsible for the reduced thickness of the UMNS as compared to the multipod seeds, but also for the formation of some cubes during the seeded growth.

In a work by Xiong *et al.*, 2D nanocrystals of Pt have been formed under different experimental conditions than the ones employed here.[52] In that work, despite Cl being present in the

precursor, 2D nanocrystals of three-fold symmetry comprising twin planes were formed. Addition of HCl in the system resulted in the formation of single crystalline nanoparticles. Despite the fact that no etching suppression was attempted, the results are in agreement with a transition from twinned to single crystalline nanocrystals upon Cl-induced etching. In general, limitation of oxidative etching can be achieved by eliminating O_2 from the reaction medium.[102,103] On the other hand the complete absence of etching possibility has been rarely exploited. Thanks to the use of halide-free precursors Rh starfish shaped nanoparticles have been obtained, while addition of HCl to the system or the use of a Cl-comprising precursor led to irregular nanocrystals.[38] Etching suppression by *in situ* removal of the Cl (or other halides), is interesting because the vast majority of precursors employed in noble metal nanoparticle syntheses contain chloride (and less often other halides). In addition, halide containing stabilizing agents such as hexadecyltrimethylammonium chloride (CTAC) or hexadecyltrimethylammonium bromide (CTAB) are routinely used, which can also afford halides in the reaction medium. Both precursor and stabilizers of this kind may induce etching effects, especially in the presence of O_2. If this possibility is not considered, the interpretation of the results can be biased.[96] A possibility of etching-free nucleation is offered by *in situ* elimination of precursor ligands that could efficiently ripen the twinned nuclei away, or by using organometallic precursors comprising non-coordinating ligands.

Selective hydrogenation of phenylacetylene

Although UMNS show high surface-to-volume ratios and thus, an increased exposure of low-coordinated sites that can provide high reactivity,[105] very few studies exist on the use of Pt nanosheets for selective hydrogenation of alkynes. Graphite intercalated Pt nanosheets were found to be active for hydrogenation of phenylacetylene (PhA), but produce as the major product ethylbenzene (EB) and not the targeted styrene (ST).[106,107] It was proposed that the active sites were the edges of the 2D metal nanosheets. Free standing, ligand-free Pt nanosheets exposing the (111) and (200) facets of fcc Pt were reported to be very active for the hydrogenation of ST to EB at 1 bar and room temperature,[108] confirming possible selectivity issues due to the strong over-hydrogenation activity of Pt. Since the use of metal Pt nanosheets in selective hydrogenation catalysis is still in its infancy, this incited us to test the Pt UMNS in the selective hydrogenation of PhA, and to benchmark them with a commercial highly dispersed catalyst 5% Pt/C (Pt nanoparticles = 1.1 nm, Fig. S16a†).

The selective hydrogenation of PhA was performed at 25 °C under 5 bar of H_2 in THF. The results of catalyst activity and selectivity for the two catalysts are presented in Fig. 5, and the TEM analyses of the fresh and spent catalysts are shown in Fig. S16.† The highly dispersed Pt/C catalyst shows slightly higher activity (Fig. 5d), but significantly lower selectivity (Fig. 5c) and stability (Fig. S16†) than the UMNS during the hydrogenation reaction. Considering the geometrical features of Pt particles in Pt/C and those of the Pt UMNS (Fig. S17†), the Pt/C catalyst exhibits a much higher proportion of surface Pt atoms. Thus, the activities measured for these two catalysts indicate that the Pt UMNS surface sites is higher. Notably, the kinetically favorable over-hydrogenation to produce EB is dominant on the Pt/C catalyst, as already reported in the literature for various carbon-supported Pt catalysts.[106,109–112] Indeed, the selectivity toward ST on Pt/C decreases dramatically from 60% at 40% conversion to 15% at 97% conversion of PhA, while for Pt UMNS, over hydrogenation is much more limited, the selectivity toward ST being 75% at 97% conversion of PhA. The high ST selectivity obtained with Pt UMNS is surprising considering the reported high activity of Pt nanosheets for ST hydrogenation.[108] However, these nanosheets were ligand-free and have different crystallographic orientation that the UMNS presented here. TEM observations performed on the spent catalysts show that severe sintering does occur for the Pt/C catalyst (final mean Pt nanoparticles size = 5.2 nm), while the structure of Pt UMNS is not affected by the reaction (Fig. S16b and d†).

The different performances of these two catalysts could be related to the presence of the ODA as the principal ligand on the Pt UMNS. Indeed, organic ligands, able to induce both steric and electronic effects on metal nanoparticles, can contribute to the tuning of the hydrogenation pathways.[113] We thus investigated the influence of the ODA ligand on the Pt/C catalyst using two different ODA concentrations. Knowing that Pt UMNS contains around 20% w/w ligands, we first added 20% w/w ODA with respect to Pt on the Pt/C catalyst (catalyst Pt-ODA1/C). As the ODA ligand can also be adsorbed on the carbon support,[114,115] we also prepared a second catalyst (Pt-ODA2/C), containing a significantly higher amount of ODA: 20% w/w ODA with respect to the Pt/C catalyst. The influence of ODA ligand on the performances of the Pt/C catalyst is shown on Fig. S18† and Fig. 5d. The addition of increasing amounts of ligand induces a decrease of activity, which could be assigned to a site blocking effect due to the N-containing ligand,[116] and an increase of selectivity towards styrene. The increase in ST selectivity upon ODA addition could arise from an electronic effect induced by the donating amine ligand, which contributes to the formation of electron-richer Pt species. Even if the XPS data of Pt UMNS indicate a moderate charge transfer from the amine to the metal, the Pt $4f_{7/2}$ peak of Pt^0 at 70.9 eV shows that Pt should be more electron rich in Pt UMNS than in Pt/C before ODA addition. Indeed, small Pt nanoparticles as the ones present in Pt/C are subjected to significant charge transfer from Pt to the carbon support, giving rise to positively charged particles.[117,118] On ODA-modified Pt/C, the dissociation of Pt–H bonds to release H_2 gas could be accelerated, due to weakened Pt–H bonds on more electron-rich Pt species.[119] We thus presume that the weakened H adsorption strength is the main reason for the observed selectivity, since ST selectivity is known to decrease with increasing hydrogen coverage.[120] Such electronic effect, which could be related to a downshift of the Pt d-band center[72] thanks to the amine ligand,[121] has already been reported for selective hydrogenation of PhA on electron rich, phosphine-

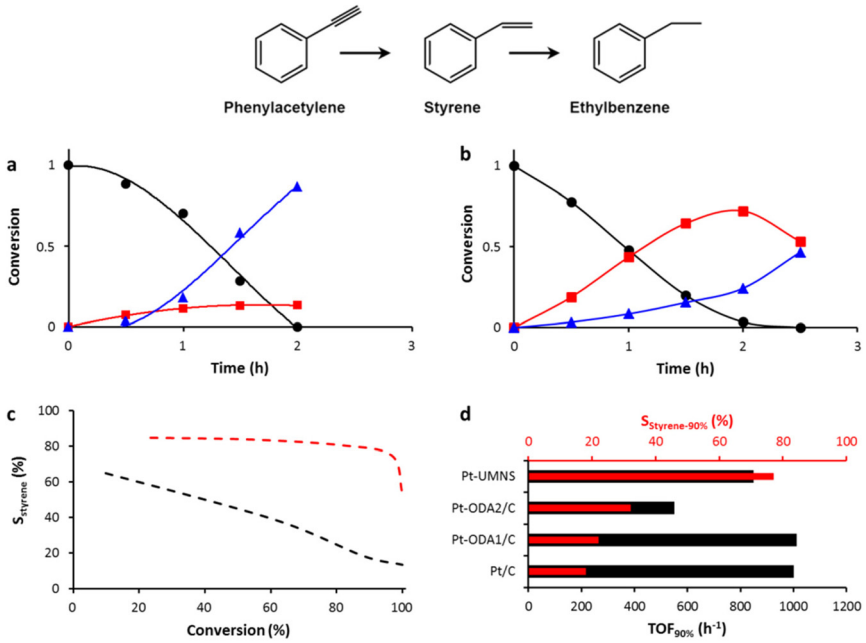

Fig. 5 Results of PhA hydrogenation on Pt catalysts. (a) Conversion obtained on Pt/C catalyst. (b) Conversion obtained on Pt UMNS catalyst (black circles PhA, red squares ST, and blue triangles EB). (c) Styrene selectivity evolution with conversion for the Pt/C (black trace) and Pt UMNS catalysts (red trace) and (d) performances of the investigated catalysts at 90% conversion.

modified Pd nanoparticles,[122] and N-graphene encapsulated Pt nanoparticles.[110] While this electronic ligand effect can contribute to the high selectivity obtained with the Pt UMNS catalyst, it cannot by itself justify the better performances of Pt UMNS, since this catalyst outperformed also the Pt-ODA2/C catalyst, both in terms of activity and selectivity (Fig. 5d). Although a direct comparison of catalytic performances is always difficult because of different experimental conditions and reactor configuration, the Pt UMNS catalyst also shows interesting performances compared to other Pt catalysts reported in the literature (Table S5†).

Further studies are needed to determine the exact nature of active sites of Pt UMNS, however, some hypotheses can be made on the basis of our results and from the analysis of the literature. First, carbon supported Pt nanoparticles are active for PhA hydrogenation but not selective for ST formation. These small particles should present, according to their size, different proportion of facets and edges. For 1.1 nm particles, a cubo-octahedron model predicts 75% of edge sites and 25% of (111) facets.[123] Second, it has been shown, that in PhA hydrogenation, ligand-free Pt nanosheets exposing the {111} and {200} type facets are very active for ST hydrogenation to EB, suggesting a low selectivity to ST.[108] Third, ligand-free Pt nanosheets intercalated between graphene layers, presenting mainly edges, were also poorly selective for PhA hydrogenation.[106,107] Finally, our results suggest that the presence of ODA, in itself, is not sufficient to explain the catalytic performance. From these observations, we believe that specific sites of the Pt UMNS surface, such as ODA-decorated lateral sites could be at the origin of the high activity and selectivity of Pt UMNS. The Pt UMNS are highly dendritic and the number of lateral sites is not negligible. These electron-rich sites should be effective to transfer electrons to the π^* molecular orbitals of PhA, promoting its activation and improving catalytic activity. These sites should favor a weak π adsorption of the ST molecule,[111] rather than a strong di-σ adsorption as observed on Pt(111),[124,125] explaining the better selectivity obtained on the Pt UMNS catalyst. Finally, the role of the amino ligands is not limited to activity and selectivity enhancement, but most likely also contributes to the catalyst stability.

Conclusions

Here we have shown that crystalline UMNS of pure Pt presenting {111} basal planes can be selectively synthesized by a seed mediated approach. The most crucial point is the selective synthesis of seeds comprising at least a twin plane, which depends on the possibility to suppress the etching process taking place during the early nucleation step, which is detrimental for the stabilization of twinned seeds. Upon introduction of an excess of Na(acac) in the reaction medium, and due to the formation of NaCl, the chloride present on the $PtCl_2$ precursor is efficiently removed from the reaction, switching off the possibility of efficient oxidative etching, which would otherwise favor the formation of thermodynamically stable defect-free nuclei that evolve to cuboids. These results suggest that when twinned seeds are pursued, chloride containing precursors, which are widely employed for the synthesis of metal

nanostructures, should be avoided. For this step, for which preservation of the initial defect comprising nuclei is crucial, *in situ* halide elimination or the use of organometallic precursors bearing ligands that upon hydrogenation/decomposition are converted to non-coordinating species, could offer an advantage. The use of $Pt(acac)_2$ as the growth precursor allows a mild ripening that accounts for the final shape of the UMNS. The UMNS synthesized here have been studied in the selective hydrogenation of phenylacetylene exhibiting high activity and high selectivity to styrene, even at high conversion.

Author contributions

D. Yi: investigation, conceptualization, writing – original draft, visualization; C. Marcelot, I. Romana, M. Tassé, L. Peres, N. Ratel Ramond, P. Decorse: investigation, visualization, writing – review and editing; P.-F. Fazzini: supervision, visualization; B. Warot Fonrose: supervision, resources, funding acquisition, writing – review and editing; G. Viau: supervision, visualization, writing – review and editing, P. Serp, K. Soulantica: conceptualization, supervision, funding acquisition, writing – review and editing.

Conflicts of interest

The authors declare that they have no conflicts of interest.

Acknowledgements

The authors thank the EUR grant NanoX ANR-17-EURE-0009 for financial support in the framework of the "Programme des Investissements d'Avenir" through the project CaSh. L. Peres thanks the University of Toulouse for financial support. The authors thank Angélique Gillet, Simon Cayez and Adeline Pham for technical support.

References

1 H. Zhang, *ACS Nano*, 2015, **9**, 9451–9469.
2 Z. Fan, X. Huang, C. Tan and H. Zhang, *Chem. Sci.*, 2015, **6**, 95–111.
3 Y. Chen, Z. Fan, Z. Zhang, W. Niu, C. Li, N. Yang, B. Chen and H. Zhang, *Chem. Rev.*, 2018, **118**, 6409–6455.
4 Y. Pei, L. Huang, J. Wang, L. Han, S. Li, S. Zhang and H. Zhang, *Nanotechnology*, 2019, **30**, 222001.
5 T. Wang, M. Park, Q. Yu, J. Zhang and Y. Yang, *Mater. Today Adv.*, 2020, **8**, 100092.
6 H. Duan, N. Yan, R. Yu, C.-R. Chang, G. Zhou, H.-S. Hu, H. Rong, Z. Niu, J. Mao, H. Asakura, T. Tanaka, P. J. Dyson, J. Li and Y. Li, *Nat. Commun.*, 2014, **5**, 3093.
7 A.-X. Yin, W.-C. Liu, J. Ke, W. Zhu, J. Gu, Y.-W. Zhang and C.-H. Yan, *J. Am. Chem. Soc.*, 2012, **134**, 20479–20489.
8 Q. Yu and Y. Yang, *ChemNanoMat*, 2020, **6**, 1683–1711.
9 M. A. Z. G. Sial, M. A. U. Din and X. Wang, *Chem. Soc. Rev.*, 2018, **47**, 6175–6200.
10 S. R. Beeram and F. P. Zamborini, *J. Am. Chem. Soc.*, 2009, **131**, 11689–11691.
11 X. Huang, S. Tang, X. Mu, Y. Dai, G. Chen, Z. Zhou, F. Ruan, Z. Yang and N. Zheng, *Nat. Nanotechnol.*, 2011, **6**, 28–32.
12 S. Tang, M. Chen and N. Zheng, *Small*, 2014, **10**, 3139–3144.
13 Y. Feng, Q. Shao, F. Lv, L. Bu, J. Guo, S. Guo and X. Huang, *Adv. Sci.*, 2020, **7**, 1800178.
14 H. Tao, Y. Gao, N. Talreja, F. Guo, J. Texter, C. Yan and Z. Sun, *J. Mater. Chem. A*, 2017, **5**, 7257–7284.
15 L. Zhao, C. Xu, H. Su, J. Liang, S. Lin, L. Gu, X. Wang, M. Chen and N. Zheng, *Adv. Sci.*, 2015, **2**, 1500100.
16 Y. Dai, S. Liu and N. Zheng, *J. Am. Chem. Soc.*, 2014, **136**, 5583–5586.
17 L. Dai, Y. Zhao, Q. Qin, X. Zhao, C. Xu and N. Zheng, *ChemNanoMat*, 2016, **2**, 776–780.
18 N. Yang, H. Cheng, X. Liu, Q. Yun, Y. Chen, B. Li, B. Chen, Z. Zhang, X. Chen, Q. Lu, J. Huang, Y. Huang, Y. Zong, Y. Yang, L. Gu and H. Zhang, *Adv. Mater.*, 2018, **30**, 1803234.
19 Z. Huang, S. Li, B. Xu, F. Yan, G. Yuan and H. Liu, *Small*, 2021, **17**, 2006624.
20 M. Luo, *Mater. Today*, 2019, **23**, 45–56.
21 S. E. Skrabalak, *Acc. Mater. Res.*, 2021, **2**, 621–629.
22 Y. Xia, Y. Xiong, B. Lim and S. E. Skrabalak, *Angew. Chem., Int. Ed.*, 2009, **48**, 60–103.
23 V. Germain, J. Li, D. Ingert, Z. L. Wang and M. P. Pileni, *J. Phys. Chem. B*, 2003, **107**, 8717–8720.
24 C. Lofton and W. Sigmund, *Adv. Funct. Mater.*, 2005, **15**, 1197–1208.
25 Y. Xiong, I. Washio, J. Chen, H. Cai, Z.-Y. Li and Y. Xia, *Langmuir*, 2006, **22**, 8563–8570.
26 A. I. Kirkland, D. A. Jefferson, D. G. Duff, P. P. Edwards, I. Gameson, B. F. G. Johnson and D. J. Smith, *Proc. R. Soc. London, Ser. A*, 1993, **440**, 589–609.
27 P. Hartman, *Z. Kristallogr. – Cryst. Mater.*, 1956, **107**, 225–237.
28 R. Jagannathan, R. V. Mehta, J. A. Timmons and D. L. Black, *Phys. Rev. B: Condens. Matter Mater. Phys.*, 1993, **48**, 13261–13265.
29 J. E. Millstone, S. J. Hurst, G. S. Métraux, J. I. Cutler and C. A. Mirkin, *Small*, 2009, **5**, 646–664.
30 Y. Xia, K. D. Gilroy, H.-C. Peng and X. Xia, *Angew. Chem., Int. Ed.*, 2017, **56**, 60–95.
31 Y. Wang, J. He, C. Liu, W. H. Chong and H. Chen, *Angew. Chem., Int. Ed.*, 2015, **54**, 2022–2051.
32 Y. Wang, H.-C. Peng, J. Liu, C. Z. Huang and Y. Xia, *Nano Lett.*, 2015, **15**, 1445–1450.
33 Q. N. Nguyen, R. Chen, Z. Lyu and Y. Xia, *Inorg. Chem.*, 2021, **60**, 4182–4197.
34 R. Long, S. Zhou, B. J. Wiley and Y. Xiong, *Chem. Soc. Rev.*, 2014, **43**, 6288–6310.

35 Y. Zheng, J. Zeng, A. Ruditskiy, M. Liu and Y. Xia, *Chem. Mater.*, 2014, **26**, 22–33.
36 M. N. O'Brien, M. R. Jones, K. A. Brown and C. A. Mirkin, *J. Am. Chem. Soc.*, 2014, **136**, 7603–7606.
37 Y. Xiong and Y. Xia, *Adv. Mater.*, 2007, **19**, 3385–3391.
38 H. Zhang, X. Xia, W. Li, J. Zeng, Y. Dai, D. Yang and Y. Xia, *Angew. Chem., Int. Ed.*, 2010, **49**, 5296–5300.
39 Y. Tang and M. Ouyang, *Nat. Mater.*, 2007, **6**, 754–759.
40 Z. Li, J.-Y. Fu, Y. Feng, C.-K. Dong, H. Liu and X.-W. Du, *Nat. Catal.*, 2019, **2**, 1107–1114.
41 X. Sun, K. Jiang, N. Zhang, S. Guo and X. Huang, *ACS Nano*, 2015, **9**, 7634–7640.
42 Y. Yang, J. Wu, X. Wang, Q. Guo, X. Liu, W. Sun, Y. Wei, Y. Huang, Z. Lan, M. Huang, J. Lin, H. Chen and Z. Wei, *Adv. Mater.*, 2020, **32**, 1904347.
43 Q. Zhu, Z. Pan, Z. Zhao, G. Cao, L. Luo, C. Ni, H. Wei, Z. Zhang, F. Sansoz and J. Wang, *Nat. Commun.*, 2021, **12**, 558.
44 Z. R. Ramadhan, A. R. Poerwoprajitno, S. Cheong, R. F. Webster, P. V. Kumar, S. Cychy, L. Gloag, T. M. Benedetti, C. E. Marjo, M. Muhler, D.-W. Wang, J. J. Gooding, W. Schuhmann and R. D. Tilley, *J. Am. Chem. Soc.*, 2022, **144**, 11094–11098.
45 S. Maksimuk, X. Teng and H. Yang, *J. Phys. Chem. C*, 2007, **111**, 14312–14319.
46 S. Maksimuk, X. Teng and H. Yang, *Phys. Chem. Chem. Phys.*, 2006, **8**, 4660–4663.
47 L. Ruan, C.-Y. Chiu, Y. Li and Y. Huang, *Nano Lett.*, 2011, **11**, 3040–3046.
48 J. L. Elechiguerra, L. Larios-Lopez and M. Jose-Yacaman, *Appl. Phys. A*, 2006, **84**, 11–19.
49 J. Chen, T. Herricks and Y. Xia, *Angew. Chem., Int. Ed.*, 2005, **44**, 2589–2592.
50 T. Herricks, J. Chen and Y. Xia, *Nano Lett.*, 2004, **4**, 2367–2371.
51 S. Kibey, J. B. Liu, D. D. Johnson and H. Sehitoglu, *Acta Mater.*, 2007, **55**, 6843–6851.
52 L. Ma, C. Wang, M. Gong, L. Liao, R. Long, J. Wang, D. Wu, W. Zhong, M. J. Kim, Y. Chen, Y. Xie and Y. Xiong, *ACS Nano*, 2012, **6**, 9797–9806.
53 L. Bu, N. Zhang, S. Guo, X. Zhang, J. Li, J. Yao, T. Wu, G. Lu, J.-Y. Ma, D. Su and X. Huang, *Science*, 2016, **354**, 1410–1414.
54 W. Wang, X. Zhang, Y. Zhang, X. Chen, J. Ye, J. Chen, Z. Lyu, X. Chen, Q. Kuang, S. Xie and Z. Xie, *Nano Lett.*, 2020, **20**, 5458–5464.
55 F. Saleem, Z. Zhang, B. Xu, X. Xu, P. He and X. Wang, *J. Am. Chem. Soc.*, 2013, **135**, 18304–18307.
56 M. Shirai, K. Igeta and M. Arai, *Chem. Commun.*, 2000, 623–624.
57 Y.-R. Hong, S. Dutta, S. W. Jang, O. F. Ngome Okello, H. Im, S.-Y. Choi, J. W. Han and I. S. Lee, *J. Am. Chem. Soc.*, 2022, **144**, 9033–9043.
58 H. Kawasaki, M. Uota, T. Yoshimura, D. Fujikawa, G. Sakai, M. Annaka and T. Kijima, *Langmuir*, 2005, **21**, 11468–11473.
59 G. Sakai, T. Yoshimura, S. Isohata, M. Uota, H. Kawasaki, T. Kuwahara, D. Fujikawa and T. Kijima, *Adv. Mater.*, 2007, **19**, 237–241.
60 T. Kijima, Y. Nagatomo, H. Takemoto, M. Uota, D. Fujikawa, Y. Sekiya, T. Kishishita, M. Shimoda, T. Yoshimura, H. Kawasaki and G. Sakai, *Adv. Funct. Mater.*, 2009, **19**, 545–553.
61 D. Xu, H. Lv, H. Jin, Y. Liu, Y. Ma, M. Han and B. Liu, *J. Phys. Chem. Lett.*, 2019, **10**, 663–671.
62 Y. Song, Y. Yang, C. J. Medforth, E. Pereira, A. K. Singh, H. Xu, Y. Jiang, C. J. Brinker, F. van Swol and J. A. Shelnutt, *J. Am. Chem. Soc.*, 2004, **126**, 635–645.
63 Y. Song, W. A. Steen, D. Peña, Y.-B. Jiang, C. J. Medforth, Q. Huo, J. L. Pincus, Y. Qiu, D. Y. Sasaki, J. E. Miller and J. A. Shelnutt, *Chem. Mater.*, 2006, **18**, 2335–2346.
64 Y. Song, M. A. Hickner, S. R. Challa, R. M. Dorin, R. M. Garcia, H. Wang, Y.-B. Jiang, P. Li, Y. Qiu, F. van Swol, C. J. Medforth, J. E. Miller, T. Nwoga, K. Kawahara, W. Li and J. A. Shelnutt, *Nano Lett.*, 2009, **9**, 1534–1539.
65 Y. Song, R. M. Dorin, R. M. Garcia, Y.-B. Jiang, H. Wang, P. Li, Y. Qiu, F. van Swol, J. E. Miller and J. A. Shelnutt, *J. Am. Chem. Soc.*, 2008, **130**, 12602–12603.
66 E. Zhu, X. Yan, S. Wang, M. Xu, C. Wang, H. Liu, J. Huang, W. Xue, J. Cai, H. Heinz, Y. Li and Y. Huang, *Nano Lett.*, 2019, **19**, 3730–3736.
67 H. Liu, P. Zhong, K. Liu, L. Han, H. Zheng, Y. Yin and C. Gao, *Chem. Sci.*, 2018, **9**, 398–404.
68 L. Peres, D. Yi, S. Bustos-Rodriguez, C. Marcelot, A. Pierrot, P.-F. Fazzini, I. Florea, R. Arenal, L.-M. Lacroix, B. Warot-Fonrose, T. Blon and K. Soulantica, *Nanoscale*, 2018, **10**, 22730–22736.
69 B. Lim, J. Wang, P. H. C. Camargo, M. Jiang, M. J. Kim and Y. Xia, *Nano Lett.*, 2008, **8**, 2535–2540.
70 J. A. Delgado, O. Benkirane, C. Claver, D. Curulla-Ferré and C. Godard, *Dalton Trans.*, 2017, **46**, 12381–12403.
71 S. A. Nikolaev, L. N. Zanaveskin, V. V. Smirnov, V. A. Averyanov and K. L. Zanaveskin, *Russ. Chem. Rev.*, 2009, **78**, 231–247.
72 Z. Wang, A. Garg, L. Wang, H. He, A. Dasgupta, D. Zanchet, M. J. Janik, R. M. Rioux and Y. Román-Leshkov, *ACS Catal.*, 2020, **10**, 6763–6770.
73 C. Salzemann, J. Urban, I. Lisiecki and M.-P. Pileni, *Adv. Funct. Mater.*, 2005, **15**, 1277–1284.
74 P. Liu, R. Qin, G. Fu and N. Zheng, *J. Am. Chem. Soc.*, 2017, **139**, 2122–2131.
75 J. J. Benítez, M. A. San-Miguel, S. Domínguez-Meister, J. A. Heredia-Guerrero and M. Salmeron, *J. Phys. Chem. C*, 2011, **115**, 19716–19723.
76 J. Oviedo, M. A. San-Miguel, J. A. Heredia-Guerrero and J. J. Benítez, *J. Phys. Chem. C*, 2012, **116**, 7099–7105.
77 M. Siemer, G. Tomaschun, T. Klüner, P. Christopher and K. Al-Shamery, *ACS Appl. Mater. Interfaces*, 2020, **12**, 27765–27776.
78 X. Fu, Y. Wang, N. Wu, L. Gui and Y. Tang, *J. Colloid Interface Sci.*, 2001, **243**, 326–330.

79 S. Carenco, S. Labouille, S. Bouchonnet, C. Boissière, X.-F. Le Goff, C. Sanchez and N. Mézailles, *Chem. – Eur. J.*, 2012, **18**, 14165–14173.
80 R. K. Blundell and P. Licence, *Phys. Chem. Chem. Phys.*, 2014, **16**, 15278–15288.
81 H. Karhu, A. Kalantar, I. J. Väyrynen, T. Salmi and D. Y. Murzin, *Appl. Catal., A*, 2003, **247**, 283–294.
82 J. A. Spencer, Y.-C. Wu, L. McElwee-White and D. H. Fairbrother, *J. Am. Chem. Soc.*, 2016, **138**, 9172–9182.
83 X. Zhu, B. Cheng, J. Yu and W. Ho, *Appl. Surf. Sci.*, 2016, **364**, 808–814.
84 N. Job, M. Chatenet, S. Berthon-Fabry, S. Hermans and F. Maillard, *J. Power Sources*, 2013, **240**, 294–305.
85 M. Hara, K. Asami, K. Hashimoto and T. Masumoto, *Electrochim. Acta*, 1983, **28**, 1073–1081.
86 B. C. Beard, *Surf. Sci. Spectra*, 1993, **2**, 91–96.
87 T. Weiss, J. Warneke, V. Zielasek, P. Swiderek and M. Bäumer, *J. Vac. Sci. Technol., A*, 2016, **34**, 041515.
88 N. T. Xuyen, H. K. Jeong, G. Kim, K. P. So, K. H. An and Y. H. Lee, *J. Mater. Chem.*, 2009, **19**, 1283–1288.
89 J. Ederer, P. Janoš, P. Ecorchard, J. Tolasz, V. Štengl, H. Beneš, M. Perchacz and O. Pop-Georgievski, *RSC Adv.*, 2017, **7**, 12464–12473.
90 A. Artemenko, A. Shchukarev, P. Štenclová, T. Wågberg, J. Segervald, X. Jia and A. Kromka, *IOP Conf. Ser.: Mater. Sci. Eng.*, 2021, **1050**, 012001.
91 M. Kehrer, J. Duchoslav, A. Hinterreiter, M. Cobet, A. Mehic, T. Stehrer and D. Stifter, *Plasma Processes Polym.*, 2019, **16**, 1800160.
92 A. Funatsu, H. Tateishi, K. Hatakeyama, Y. Fukunaga, T. Taniguchi, M. Koinuma, H. Matsuura and Y. Matsumoto, *Chem. Commun.*, 2014, **50**, 8503–8506.
93 X. Yin, M. Shi, J. Wu, Y.-T. Pan, D. L. Gray, J. A. Bertke and H. Yang, *Nano Lett.*, 2017, **17**, 6146–6150.
94 R. K. Sodhi, A. Changotra and S. Paul, *Catal. Lett.*, 2014, **144**, 1819–1831.
95 S. A. De Pascali, P. Papadia, S. Capoccia, L. Marchiò, M. Lanfranchi, A. Ciccarese and F. P. Fanizzi, *Dalton Trans.*, 2009, 7786–7795.
96 S. E. Lohse, N. D. Burrows, L. Scarabelli, L. M. Liz-Marzán and C. J. Murphy, *Chem. Mater.*, 2014, **26**, 34–43.
97 K. D. Gilroy, J. Puibasset, M. Vara and Y. Xia, *Angew. Chem., Int. Ed.*, 2017, **56**, 8647–8651.
98 C. R. Laramy, L.-K. Fong, M. R. Jones, M. N. O'Brien, G. C. Schatz and C. A. Mirkin, *Chem. Phys. Lett.*, 2017, **683**, 389–392.
99 J. S. Du, W. Zhou, S. M. Rupich and C. A. Mirkin, *Angew. Chem., Int. Ed.*, 2021, **60**, 6858–6863.
100 R. R. Grinstead and J. C. Davis, *J. Phys. Chem.*, 1968, **72**, 1630–1638.
101 S. Cheong, J. Watt, B. Ingham, M. F. Toney and R. D. Tilley, *J. Am. Chem. Soc.*, 2009, **131**, 14590–14595.
102 C. J. Wang, E. F. Shapiro and M. L. Personick, in *Reference Module in Materials Science and Materials Engineering*, Elsevier, 2022, p. B9780128224250000000.
103 N. Zettsu, J. M. McLellan, B. Wiley, Y. Yin, Z.-Y. Li and Y. Xia, *Angew. Chem., Int. Ed.*, 2006, **45**, 1288–1292.
104 S. Ghosh and L. Manna, *Chem. Rev.*, 2018, **118**, 7804–7864.
105 C. Cao, Q. Xu and Q.-L. Zhu, *Chem. Catal.*, 2022, **2**, 693–723.
106 M. Shirai, B. M. Bhanage, H. Senboku, S. Fujita and M. Arai, *J. Jpn. Pet. Inst.*, 2002, **45**, 420–421.
107 M. Shirai, *Chem. Rec.*, 2019, **19**, 1263–1271.
108 T.-W. Chen, D.-W. Pang, J.-X. Kang, D.-F. Zhang and L. Guo, *Front. Chem.*, 2022, **9**, 818900.
109 S. Galvagno, Z. Poltarzewski, A. Donato, G. Neri and R. Pietropaolo, *J. Mol. Catal.*, 1986, **35**, 365–375.
110 L. Xia, D. Li, J. Long, F. Huang, L. Yang, Y. Guo, Z. Jia, J. Xiao and H. Liu, *Carbon*, 2019, **145**, 47–52.
111 M. Hu, L. Jin, Y. Dang, S. L. Suib, J. He and B. Liu, *Front. Chem.*, 2020, **8**, 581512.
112 Y. Liu, W. Guo, X. Li, P. Jiang, N. Zhang and M. Liang, *ACS Appl. Nano Mater.*, 2021, **4**, 5292–5300.
113 K. Liu, R. Qin and N. Zheng, *J. Am. Chem. Soc.*, 2021, **143**, 4483–4499.
114 L. Peres, M. R. Axet, D. Yi, P. Serp and K. Soulantica, *Catal. Today*, 2020, **357**, 166–175.
115 D. Das and B. C. Meikap, *Indian Chem. Eng.*, 2021, **63**, 435–447.
116 M. Crespo-Quesada, R. R. Dykeman, G. Laurenczy, P. J. Dyson and L. Kiwi-Minsker, *J. Catal.*, 2011, **279**, 66–74.
117 Y. Peng, B. Lu, N. Wang, L. Li and S. Chen, *Phys. Chem. Chem. Phys.*, 2017, **19**, 9336–9348.
118 I. C. Gerber and P. Serp, *Chem. Rev.*, 2020, **120**, 1250–1349.
119 L.-H. Sun, Q.-Y. Li, S.-N. Zhang, D. Xu, Z.-H. Xue, H. Su, X. Lin, G.-Y. Zhai, P. Gao, S.-I. Hirano, J.-S. Chen and X.-H. Li, *Angew. Chem., Int. Ed.*, 2021, **60**, 25766–25770.
120 B. A. Wilhite, M. J. McCready and A. Varma, *Ind. Eng. Chem. Res.*, 2002, **41**, 3345–3350.
121 Y.-H. Chung, D. Y. Chung, N. Jung and Y.-E. Sung, *J. Phys. Chem. Lett.*, 2013, **4**, 1304–1309.
122 M. Guo, H. Li, Y. Ren, X. Ren, Q. Yang and C. Li, *ACS Catal.*, 2018, **8**, 6476–6485.
123 C. M. Zalitis, A. R. Kucernak, J. Sharman and E. Wright, *J. Mater. Chem. A*, 2017, **5**, 23328–23338.
124 G. Polzonetti, V. Carravetta, M. V. Russo, G. Contini, P. Parent and C. Laffon, *J. Electron Spectrosc. Relat. Phenom.*, 1999, **98–99**, 175–187.
125 Y. Jin, P. Wang, X. Mao, S. Liu, L. Li, L. Wang, Q. Shao, Y. Xu and X. Huang, *Angew. Chem., Int. Ed.*, 2021, **60**, 17430–17434.